

Cosmological evolution of atomic gas and implications for 21 cm H I absorption

Robert Braun

CSIRO Astronomy and Space Science, PO Box 76, Epping, NSW 1710, Australia

Robert.Braun@csiro.au

ABSTRACT

Galaxy disks are shown to contain a significant population of atomic clouds of 100 pc linear size which are self-opaque in the 21 cm transition. These objects have H I column densities as high as 10^{23}cm^{-2} and contribute to a global opacity correction factor of 1.34 ± 0.05 that applies to the integrated 21 cm emission to obtain a total H I mass estimate. High resolution, opacity-corrected images of the nearest external galaxies have been used to form a robust redshift zero distribution function of H I, $f(N_{HI}, X, z = 0)$, the probability of encountering a specific H I column density along random lines-of-sight per unit comoving distance. This is contrasted with previously published determinations of $f(N_{HI}, X)$ at $z = 1$ and 3 . A systematic decline of moderate column density ($18 < \log(N_{HI}) < 21$) H I is observed with decreasing redshift that corresponds to a decline in surface area of such gas by a factor of five since $z = 3$. The number of equivalent Damped Lyman Alpha absorbers ($\log(N_{HI}) > 20.3$) has also declined systematically over this redshift interval by a similar amount, while the cosmological mass density in such systems has declined by only a factor of two to its current, opacity corrected value of $\Omega_{HI}^{DLA}(z=0) = 5.4\pm 0.9\times 10^{-4}$.

We utilise the tight, but strongly non-linear dependance of 21 cm absorption opacity on column density at $z = 0$ to transform our high resolution H I images into ones of 21 cm absorption opacity. These images are used to calculate distribution and pathlength functions of integrated 21 cm opacity. We suggest that that this $z = 0$ calibration may also apply at higher redshift. In this case, the incidence of deep 21 cm absorption systems is predicted to show very little evolution with redshift, while that of faint absorbers should decline by a factor of five between $z = 3$ and the present. We explicitly consider the effects of H I absorption against background sources that are extended relative to the 100 pc intervening absorber size scale. Extended background sources result in dramatically altered distribution and pathlength functions which are insensitive to the predicted redshift evolution. Future surveys of 21 cm absorption will require very high angular resolution, of about 15 mas, for their unambiguous interpretation.

Subject headings: galaxies: individual (M31, M33, LMC) – galaxies: Local Group
– galaxies: ISM – galaxies: evolution – cosmology: observations – radio lines:
galaxies

1. Introduction

The 21 cm neutral hydrogen emission line has proven an extremely useful diagnostic of the interstellar medium of our own and nearby galaxies since its first observation by Ewen & Purcell (1951) and Muller & Oort (1951). And despite the fact that it was soon recognised (Hagen & McClain 1954) that this transition could have significant opacity under interstellar conditions, it has often proven convenient to neglect that possibility when estimating the total H I mass of galaxies or the statistical properties of the neutral interstellar medium. Opacity estimation is straightforward in directions toward bright, compact background continuum sources, but is considerably more challenging to determine when based on the emission spectrum alone (Rohlfs et al. 1972). A finite line opacity will cause systematic changes to the shape of emission spectra that can be used to estimate opacity for simple media and viewing geometries. Line-of-sight confusion encountered when viewing edge-on systems presents a very serious challenge to such an analysis given the likelihood for discrete features to overlap in both position and velocity. This has precluded detailed opacity modelling of the Galactic neutral hydrogen emission near and in the plane. Only by assuming a single universal effective temperature for all the H I in the Galaxy have some crude opacity corrections been made (e.g. Schmidt (1957), Henderson et al. (1982)).

The first detailed opacity modelling of the H I emission in an external galaxy has recently been undertaken by Braun et al. (2009) within M31. This was enabled by achieving 100 pc linear and 2 km s^{-1} spectral resolution at sub-Kelvin brightness sensitivity. High quality fits to individual spectra based on a physical model were possible over the majority of the disk, with the exception of those regions where the “warping” phenomenon of the outer disk leads to line-of-sight confusion. That study determined that opacity corrections could locally exceed an order of magnitude in the implied H I column density and that these resulted in a 30% increase in the global H I mass estimate. But how representative are these values and to what extent are they influenced by the relatively high mean inclination, $i = 78^\circ$, of the M31 disk or the finite spatial resolution?

In this paper we extend the analysis of Braun et al. (2009) to the two other external galaxies for which the requisite physical resolution and sensitivity in the 21 cm H I emission line are available, M33 and the LMC. These galaxies have the virtue of a much more favorable disk orientation, with inclinations of about 50° and 25° respectively. The extreme proximity

of the LMC also permits linear scales as small as 15 pc to be probed with good sensitivity. Although small, this sample permits some general conclusions to be drawn regarding the statistical occurrence of opaque 21 cm H I emission and H I column densities.

We begin with a brief description of the observations and their reduction in §2 and continue with their opacity analysis in §3. In §4 we present a statistical analysis of the occurrence of opacity corrected H I column density within all three galaxies and put these in a cosmological context by considering the prospects for detection of intervening 21 cm H I absorbers toward distant background sources. We assume a distance to M31 of 785 kpc (McConnachie et al. 2005), to M33 of 794 kpc (McConnachie et al. 2004) and to the LMC of 51 kpc (Koerwer 2009) throughout. We further adopt a flat cosmological model with $\Omega_\lambda = 0.73$ and a Hubble constant of $71 \text{ km s}^{-1}\text{Mpc}^{-1}$ (Hinshaw et al. 2009).

2. Observations

2.1. M31

The observations and data reduction methods relevant to M31 are described in detail in Braun et al. (2009). The most relevant aspects are the high quality total power data obtained with the Green Bank Telescope (GBT) as described by Thilker et al. (2004) combined with a 163 pointing mosaic obtained with the Westerbork Synthesis Radio Telescope (WSRT) in its “maxi-short” configuration. The data cube used for the spectral modeling analysis had angular resolution of $30''$ (114 pc), velocity resolution of 2.27 km s^{-1} and RMS noise level of 1.0 K per channel. The relevant data attributes are summarized in Table 1.

2.2. M33

Total power observations of a $5^\circ \times 5^\circ$ region centered on M33 were carried out with the GBT during 2002 October using the same setup described by Thilker et al. (2004) for the observations of M31. Interferometric data was acquired with the Very Large Array (VLA) in 1997, 1998 and 2001 under the proposal IDs AT206 and AT268. This consisted of a six pointing mosaic in the B and CS configurations and an additional 20 pointing mosaic in the D configuration. Some early results based on the B and CS configuration data were presented in Thilker et al. (2002) while an independent reduction of all three VLA configurations has been presented by Gratier et al. (2010). Joint deconvolution of all of the VLA pointing data was carried out after inclusion of the appropriately scaled GBT total power images following the method employed for the reduction of the M31 data described in detail by Braun et al.

(2009). The data cube used for the spectral modeling analysis had angular resolution of $20''$ (77 pc), velocity resolution of 1.42 km s^{-1} and RMS noise level of 2.1 K per channel.

2.3. LMC

The observations and data reduction methods relevant to LMC are described in detail in Kim et al. (2003). The most relevant aspects are the total power data obtained with the Parkes Telescope and its Multi-Beam 21 cm receiver combined with a 1344 pointing mosaic obtained with the Australia Telescope Compact Array (ATCA) in its 750A, 750C and 750D configurations. The data cube used for the spectral modeling analysis had angular resolution of $60''$ (15 pc), velocity resolution of 1.65 km s^{-1} and RMS noise level of 2.5 K per channel.

2.4. Additional Targets

While it would be very advantageous to extend our galaxy sample beyond the Local Group targets listed above, this is beyond the capabilities of current surveys and radio telescopes.

For comparison, the THINGS survey (Walter et al. 2008) consists of H I imaging of 34 relatively nearby galaxies using multiple configurations of the VLA. Although this survey achieves an angular resolution as high as 6 arcsec, which corresponds to less than 150 pc for the thirteen THINGS galaxies within about 4 Mpc, the corresponding RMS brightness sensitivity per velocity channel varies between about 10 and 20 K at this angular resolution while the velocity resolution is too coarse for several of the galaxies (5.2 km s^{-1}) and only marginal (2.6 km s^{-1}) for the remainder. As will become apparent below, parameterised spectral fitting is only found to be viable when at least one independent velocity channel exceeds 10σ and at least five exceed 5σ . For this reason it is vital to achieve better than about 2 K brightness sensitivity over 2 km s^{-1} at the required physical resolution of about 100 pc that matches intrinsic H I structure sizes. The THINGS survey has insufficient sensitivity by a factor of between 5 and 10 for this purpose. Remedying this shortcoming would require between 25 and 100 times longer integrations, or between 250 and 1000 hours per target with the EVLA.

Another ongoing survey of nearby galaxies that might be considered of potential relevance is the HALOGAS survey of Heald et al. (2011). That survey involves relatively deep (120 hours per target) observations of a galaxy sample within about 10 Mpc. Unfortunately, as that survey is designed primarily to detect diffuse gas in the extended environments of

galaxies it has only modest physical (about 1 kpc) and velocity (4.2 km s⁻¹) resolution that make it unsuitable for parameterised spectral fitting of well-resolved structures.

3. Spectral Analysis

The method of spectral analysis has been described in detail in Braun et al. (2009). We repeat the most relevant aspects of that analysis below for clarity.

Each line profile is modeled as a spatially resolved *isothermal* H I feature in the *presence of turbulent broadening* as

$$T_B(V) = T_S\{1 - \exp[-\tau(V)]\} \quad (1)$$

with

$$\tau(V) = \frac{5.49 \times 10^{-19} N_{HI}}{T_S \sqrt{2\pi\sigma^2}} \exp\left(-0.5 \frac{V^2}{\sigma^2}\right) \quad (2)$$

where the velocity dispersion, σ , has units of km s⁻¹ and is the quadratic sum of an assumed thermal and nonthermal contribution $\sigma^2 = (\sigma_T^2 + \sigma_{NT}^2)$ with the thermal contribution given by $\sigma_T = 0.093\sqrt{T_k}$, for a kinetic temperature, T_k . Such profiles have a Gaussian shape for low ratios of the H I column density (in units of cm⁻²) to spin temperature, N_{HI}/T_S , but become increasingly flat-topped when this ratio becomes high.

We found the best-fitting model spectrum for the brightest spectral feature along each line-of-sight when the observed peak brightness temperature exceeded 10 times the RMS noise and the truncated peak (where brightnesses greater than 50% of the peak were encountered) spanned at least five independent velocity channels. The requirement for a well-sampled linewidth translates directly into one on the velocity resolution of the input galaxy data of better than about 2 km s⁻¹. The truncation was done to both isolate single spectral components from possibly blended features as well as eliminating potential broad wings from the fit. In this way, the broad wings of secondary components along the same line of sight, for example from additional warm neutral gas with $\sim 10^4$ K temperature, could be excluded from the fit. The data were compared to a pre-calculated set of model spectra spanning the range $\log(N_{HI}) = 20.0$ to 23.5 by 0.01, $\log(T_C) = 1.2$ to 3.2 by 0.01 and $\log(\sigma_{NT}) = 0.3$ to 1.5 by 0.04. A search in velocity offset was done over displacements of -4 to $+4$ by 1 km s⁻¹ with respect to the line centroid as estimated by the first moment of each truncated peak.

Only those fits with a normalized $\chi^2 = \sum_i (D_i - M_i)^2 / (N\sigma^2) < 25$ were retained; a cut-off based on the rejection level needed within M31 to exclude instances of line blending where the outer “warp” is seen in projection against the inner disk. In the case of M31 this

resulted in rejection of some 4% of the fits, while for both M33 and the LMC the fit rejection rate dropped to below 1%.

Results of the spectral fitting were recorded as images of the physical parameters, N_{HI}^{Fit} , T_S and σ_{NT} together with the integral of brightness temperature over velocity that corresponds to the column density of the fit, $\int T_B^{Fit} dV$. This allowed calculation of a total corrected column density image from,

$$N_{HI}^{Tot} = N_{HI}^{Fit} + 1.823 \times 10^{18} \left(\int T_B^{Tot} dV - \int T_B^{Fit} dV \right) \quad (3)$$

where $\int T_B^{Tot} dV$ is just the usual image of integrated emission. Those lines-of-sight with insufficient fit quality ($\chi^2 > 25$) or insufficient peak brightness and width (at least one independent velocity channel exceeding 10σ and at least five exceeding 5σ) were assumed to have negligible opacity and simply assigned the optically thin value.

4. Discussion

4.1. Opacity-corrected images and the local Ω_{HI}^{gal}

We present images of the opacity corrected neutral hydrogen column density in Figures 1–3. In contrast to images of the apparent column density, $N'_{HI} = 1.823 \times 10^{18} \int T_B dV$, which saturate below 10^{22} cm^{-2} into an almost featureless fog, there is widespread fine structure that extends to about 10^{23} cm^{-2} . It is interesting to note that comparably high H I columns have been observed in the Lyman Alpha absorption spectra of high redshift GRBs (Fynbo et al. 2009). This contrast is illustrated in Figure 4 where the corrected and apparent distributions are shown side by side for a region in the southeastern quadrant of the LMC that includes 30 Doradus (near $(\alpha, \delta) = (05:40, -69:00)$). This figure also serves to demonstrate the exceptional detail provided by the LMC linear resolution of only 15 pc. While many of the high column density features in M31 and M33 are only marginally resolved with 100 pc resolution, the majority of the LMC features are well-resolved into structures that have coherent derived properties, despite the fact that every line-of-sight has been independently fit with a model spectrum. The corrected total H I masses exceed those that follow from the assumption of negligible 21 cm opacity by factors of 1.30, 1.36 and 1.33 for M31, M33 and the LMC respectively. As noted by Braun et al. (2009), the M31 value may be biased to a lower value since some portions of the disk are confused by the warp and could not be adequately modeled. Although our sample of galaxies with opacity-corrected H I column densities is very small, it does sample both the mass density peak and the highly populated tail of the H I mass function (Zwaan et al. 2003) with apparent values of

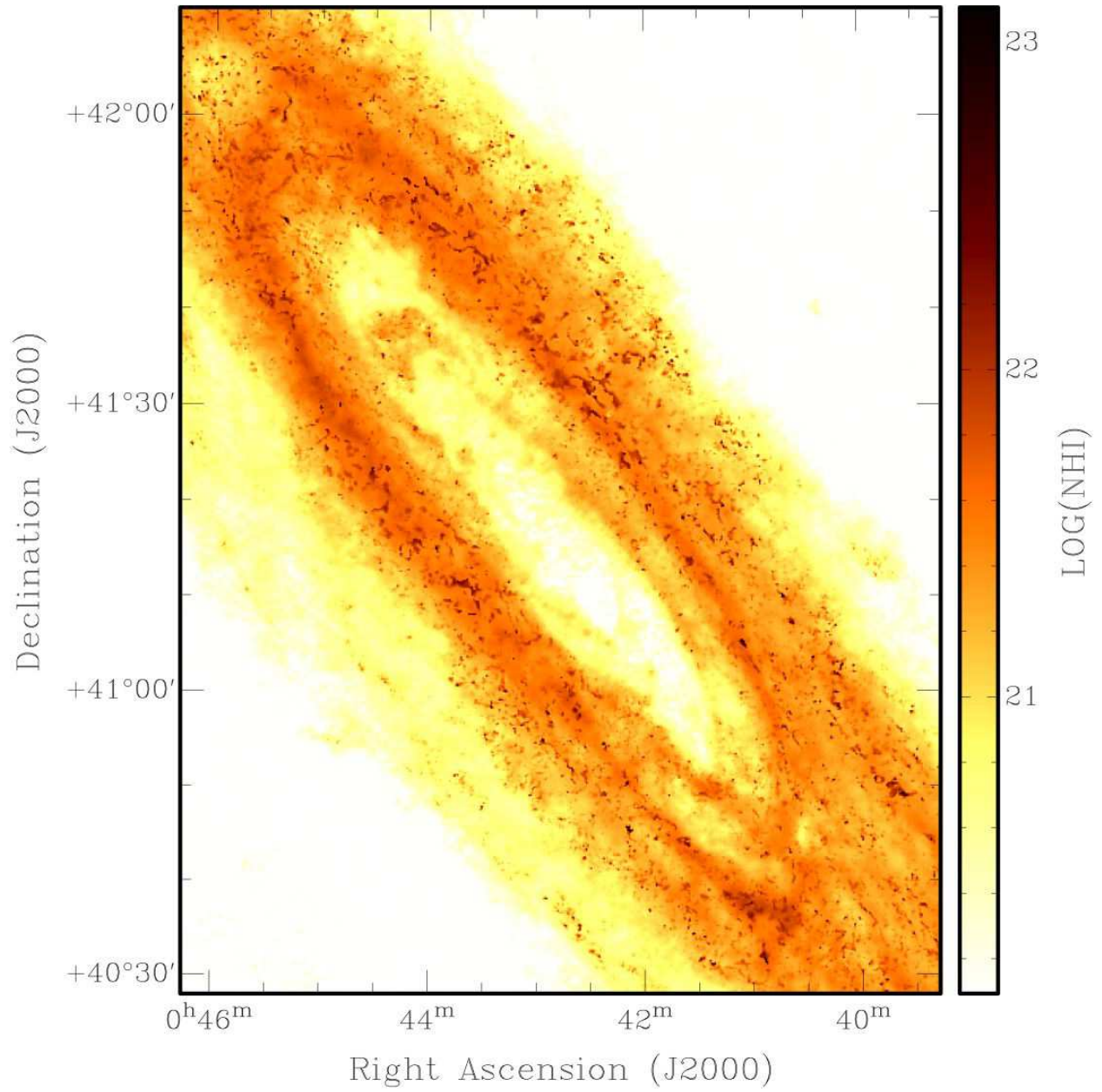


Fig. 1.— Opacity corrected neutral hydrogen column density in the inner disk of M31.

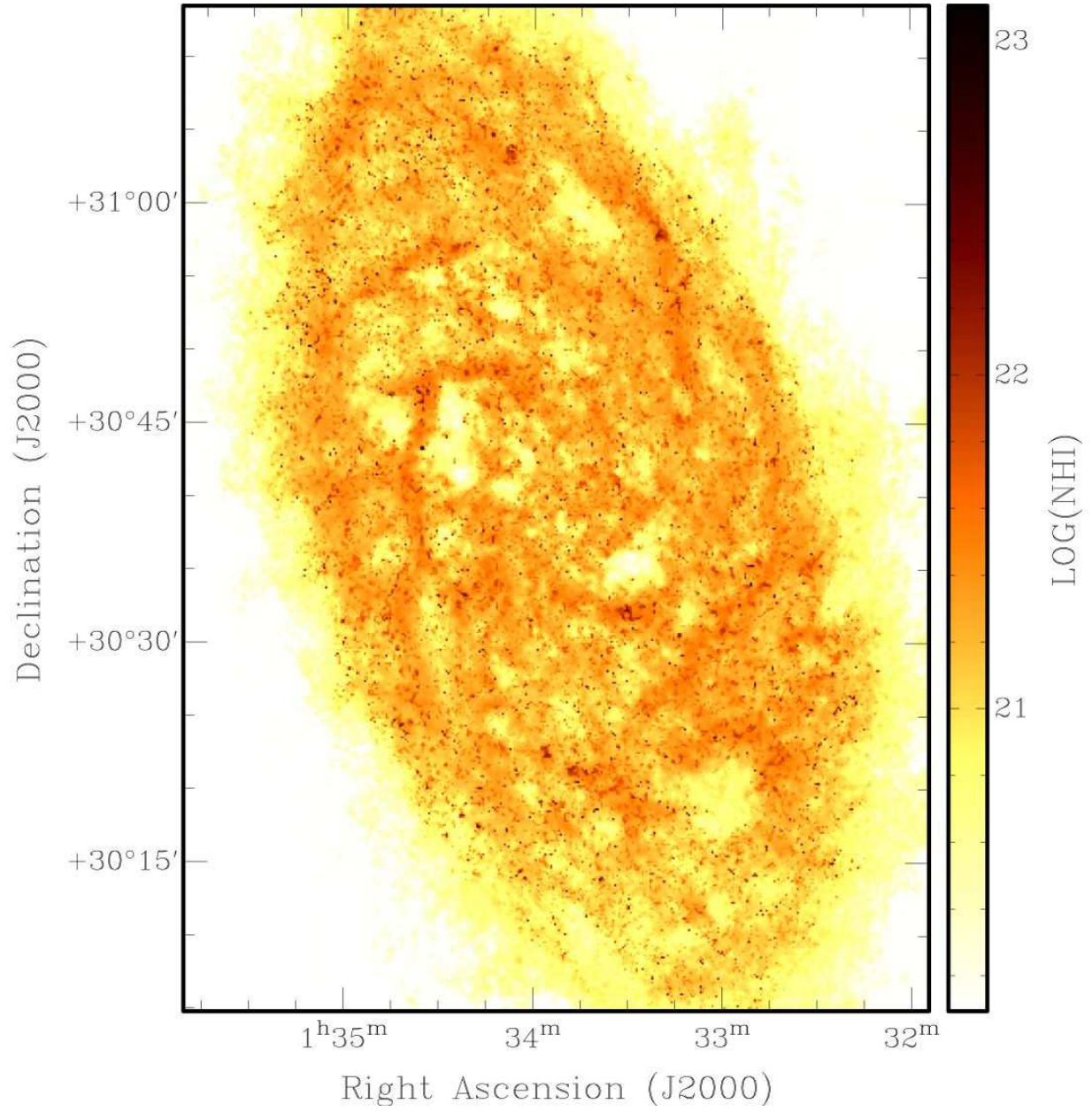


Fig. 2.— Opacity corrected neutral hydrogen column density in M33.

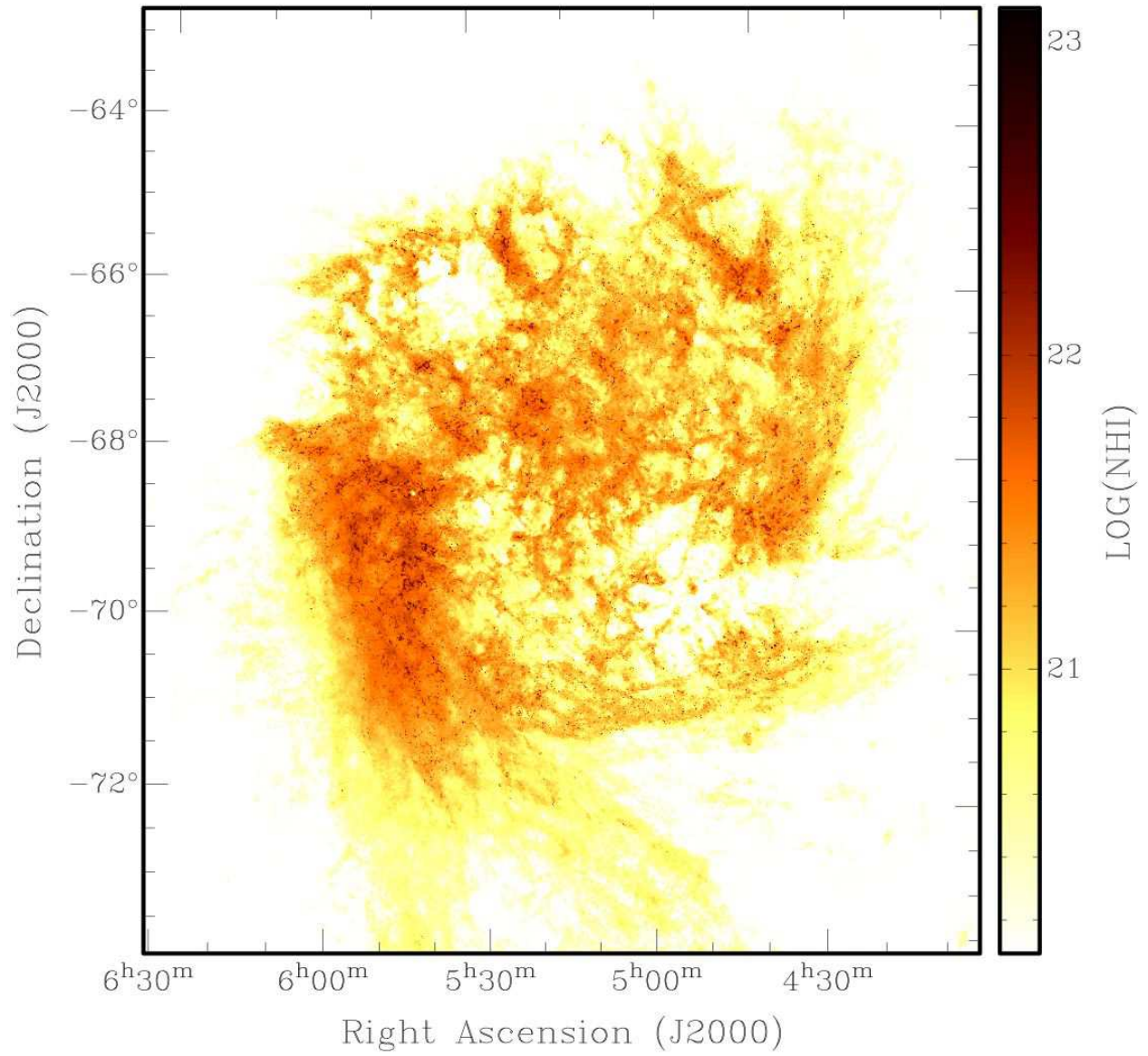


Fig. 3.— Opacity corrected neutral hydrogen column density in the LMC.

$\log(M_{HI}) = 9.77, 9.13$ and 8.61 . And while all three galaxies are of moderately late type, the same is true of about 90% of galaxies within the complete HIPASS sample (Zwaan et al. 2003) both by their contribution to the total H I mass and in terms of space density. If these global correction factors are representative of galaxies in general, they suggest that the estimated redshift zero mass density, Ω_{HI}^{gal} , determined from unbiased surveys of H I emission from galaxies in the local universe requires this magnitude of upward correction. Taking the average of the HIPASS determined value (Zwaan et al. 2003) and the recent ALFALFA value (Martin et al. 2010) after converting both to the assumed cosmology and scaling up by an opacity correction factor of 1.34 ± 0.05 yields $\Omega_{HI}^{gal}(z = 0) = 5.6 \pm 0.9 \times 10^{-4}$.

The existence of additional gas, in excess of that inferred from the published 21 cm and CO data has been previously suggested by Bernard et al. (2008) in the case of the LMC from what has been termed “excess FIR” emission. Those authors have demonstrated that the dust optical depth is enhanced in regions of the highest apparent H I column density consistent with approximately twice the total gas mass being present. The opaque 21 cm emission that we document appears to account for some 35% of this FIR excess. This cool atomic hydrogen gas will likely be closely associated with diffuse molecular hydrogen gas that may be deficient in CO emission relative to the high density, self-gravitating molecular clouds that are generally used to calibrate the CO to H₂ conversion factor (e.g. Dickman et al. 1986). A detailed analysis of atomic, molecular and dust tracers in the LMC, including our opacity-corrected H I results will be presented in Thilker et al. (2012).

4.2. H I distribution and mass density functions

It has been recognised for some time that images of 21 cm H I emission from nearby galaxies can be used to construct a distribution function that documents the probability to intercept a particular column density on a random line-of-sight. The first application of this approach (Rao & Briggs 1993) employed the assumption that the apparent H I mass was distributed smoothly over a typical H I size that depends on galaxy type. Subsequent studies (e.g. Ryan-Weber et al. (2003), Zwaan et al. (2005)) have made use of interferometric images to estimate the areal coverage of specific column densities, but even these have been limited to a median physical resolution of some 1.4 kpc and no ability to correct for 21 cm opacity effects. Most recently, Erkal et al. (2012) have used the THINGS galaxy images to this end, despite the fact that those data have only marginal resolution and inadequate sensitivity to enable resolved opacity corrections to be made, as discussed in §2.4 above. We have used the opacity corrected column density images (Figs.1–3) together with the sensitive wide-field total power 21 cm H I emission data from the combined M31/M33 system (Braun & Thilker

Table 1. Galaxy sample for spectral analysis

Name	Beam (arcsec)	Beam (pc)	ΔT_B (K)	ΔV (km s ⁻¹)	Ref
M31	30	114	2.27	1.0	1
M33	20	77	1.42	2.1	2
LMC	60	15	1.65	2.5	3

References. — (1) Braun et al. 2009; (2) Thilker et al. 2002; (3) Kim et al. 2003

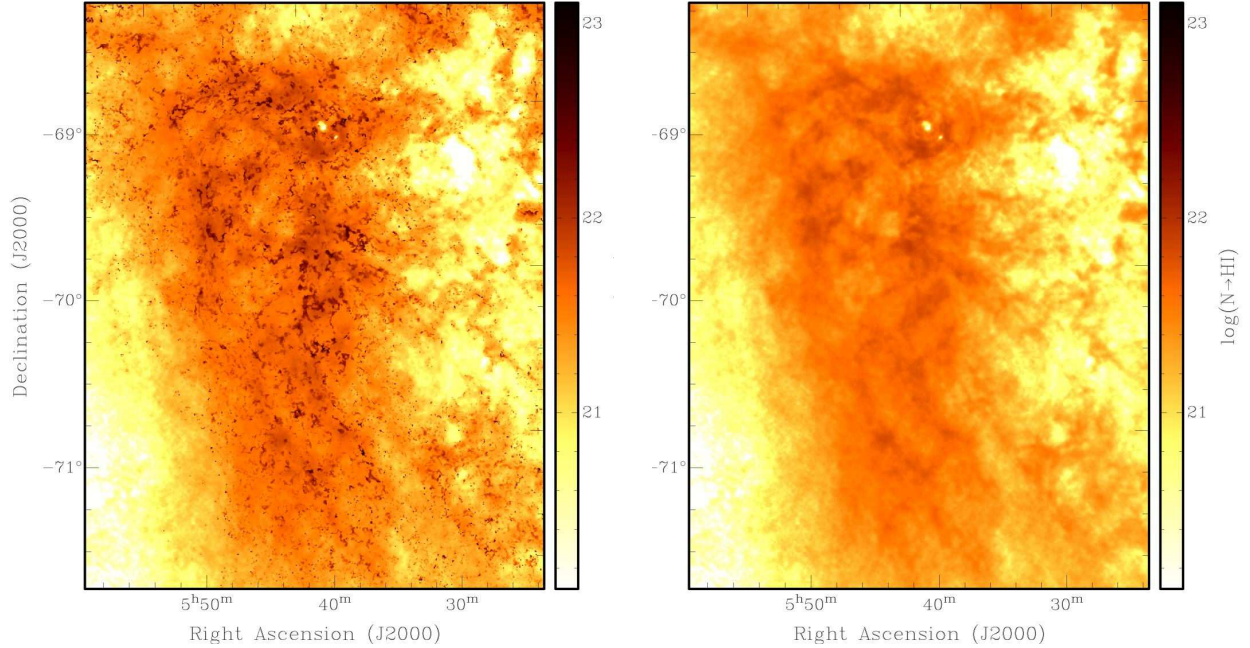


Fig. 4.— Opacity corrected (left) and apparent (right) neutral hydrogen column density in the southeastern quadrant of the LMC.

2004) and deep GBT imaging of the M31 environment (Thilker et al. 2004) to construct the H I distribution function shown in Figure 5 that spans more than six orders of magnitude in H I column density from $10^{17} - 10^{23}\text{cm}^{-2}$.

The curves in Figure 5 were calculated from,

$$f(N_{\text{HI}}, X) = \frac{c}{H_0} \frac{\rho_{av}}{\sum_i \rho_i} \sum_i \theta_i \frac{A(\log(N_{\text{HI}i}))}{N_{\text{HI}} \ln(10) d\log(N_{\text{HI}})} \quad \text{cm}^2 \quad (4)$$

where X represents unit co-moving depth along the line-of-sight,

$$dX = \frac{H_0}{H(z)} (1+z)^2 dz \quad (5)$$

and

$$\theta_i = \theta_* \ln(10) (M_i/M_*)^{\alpha+1} \exp(-M_i/M_*) \quad (6)$$

is the space density of galaxies with an *apparent* (i.e. uncorrected for opacity effects) H I mass M_i in units of $\text{Mpc}^{-3}\text{dex}^{-1}$ and $A(\log(N_{\text{HI}i}))$ is the surface area subtended by H I in the column density interval $d\log(N_{\text{HI}})$ centered on N_{HI} for galaxy i . The area is measured by counting image pixels in each column density range and multiplying by the physical area of each pixel. $\rho_i = \theta_i M_i$ is the mass density due to galaxies of type i . The HIMF parameters were taken from Zwaan et al. (2003); namely a faint-end slope, $\alpha = -1.30 \pm 0.08$, characteristic H I mass, $\log(M_*/M_\odot) = 9.84 \pm 0.06$ and normalization, $\theta_* = 7.3 \pm 1.8 \times 10^{-3} \text{Mpc}^{-3}\text{dex}^{-1}$, where $H_0 = 71 \text{km}^{-1}\text{Mpc}^{-1}$ has been assumed throughout (Hinshaw et al. 2009) and been used to rescale the HIMF parameters. The term, $\rho_{av}/\sum_i \rho_i$ in eqn. 4 is introduced to normalize our measurements for three galaxies, to the global average density of *apparent* H I in galaxies, $\rho_{av} = 5.8 \times \pm 1.0 \times 10^7 \text{M}_\odot \text{Mpc}^{-3}$, also taken from Zwaan et al. We stress that we make use of consistent quantities for this calculation, namely *apparent* galaxy H I masses and mass densities based on *apparent* mass. Alternatively, *corrected* quantities could have been used throughout.

The solid curve in Figure 5 below $\log(N_{\text{HI}}) = 18.7$ is taken from the wide-field ($60^\circ \times 30^\circ$) WSRT total power data (Braun & Thilker 2004), the curve below $\log(N_{\text{HI}}) = 19.8$ from the extended ($7^\circ \times 7^\circ$) GBT total power data of M31 (Thilker et al. 2004), while the curve above $\log(N_{\text{HI}}) = 19.5$ is that derived from the opacity corrected high resolution images presented in Figs. 1–3. For comparison, we also plot the distribution function without opacity correction as the dark dot-dash curve in the figure. The uncorrected data show an exponential upper cut-off that precludes column densities as large as 10^{22}cm^{-2} . The opacity corrected data show an approximate power law extension to the distribution above about $\log(N_{\text{HI}}) = 21.5$. We plot a power law with -3 index as the dot-dash line that provides a very good match to the measured distribution. Perhaps fortuitously, this power law index corresponds to what

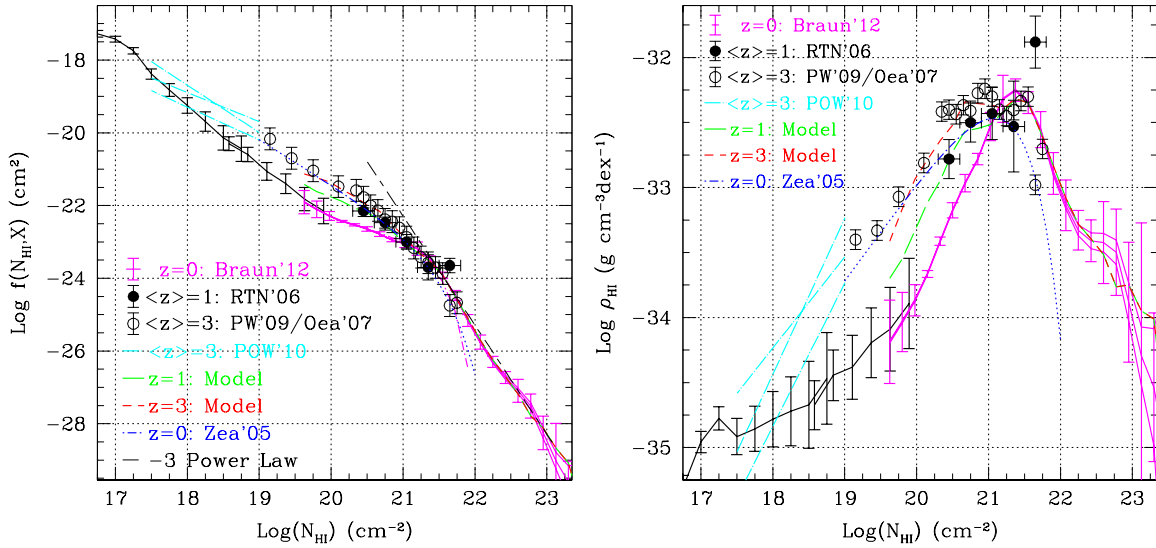


Fig. 5.— Distribution function of neutral hydrogen column density (left) and the mass density function (right). Please see Figure 6 for greater detail of the inner portion of this figure. Solid curves represent our current, $z = 0$, determination. Filled circles are used for the $\langle z \rangle = 1$ QSO absorption line data of Rao et al. (2006) and open circles for the $\langle z \rangle = 3$ QSO absorption line data of Prochaska & Wolfe (2009) and O’Meara et al. (2007). The dot-long-dash curves extend the $\langle z \rangle = 3$ data to lower N_{HI} (Prochaska et al. 2010). The dot-dash curve is the $z = 0$ determination of Zwaan et al. (2005) based on low resolution (1.4 kpc) H I emission images. The long-dashed and dashed curves represent the model we develop to represent the $\langle z \rangle = 1$ and 3 distributions. The short-dash, long-dash curve in the left panel is a -3 power law overlaid on the high N_{HI} data.

would be expected for a population of resolved thin structures with some characteristic face-on column density when viewed at random orientations, as first noted by Milgrom (1988). This may well be a plausible interpretation for observations such as presented here which resolve the atomic “skins” of what are likely to be randomly oriented clouds of molecular hydrogen on 100 pc scales within galaxy disks.

Of particular note is the magnitude of the statistical errors in our determination of $f(N_{HI}, X)$. The solid curve above $\log(N_{HI}) = 19.5$ in the figure have been plotted three times: once as measured and again with both the addition and subtraction of the statistical 1σ error calculated from the number of independent image pixels contributing to each column density bin. Only above $\log(N_{HI}) = 22.5$ can these curves be distinguished from one another at all. The detailed shape of the combined curve above $\log(N_{HI}) = 19.5$ is also reproduced in detail by the three galaxies individually, despite the fact that they represent different Hubble types and H I masses; ranging from SB(s)m, to SA(s)cd to SA(s)b and spanning an uncorrected $\log(M_{HI}) = 8.6 - 9.8$. From Figure 13 of Zwaan et al. (2003) it is apparent that galaxies of these relatively late types contribute about 90% to the H I mass function in terms of both total mass and galaxy space density. The degree of inter-galaxy consistency is demonstrated with the error bars on the solid curve which represent RMS differences of the distribution functions of the three individual galaxies with respect to the combined $f(N_{HI}, X)$. What hasn't been included in these error bars is the systematic error due to the uncertainty in the normalisation for galaxy space density, θ_* (and hence ρ_{HI}), of about 0.1 dex. Errors in the normalisation would result in a vertical shift of the entire distribution function, but would not otherwise change the shape.

We plot the parameterised fit to the H I distribution function of Zwaan et al. (2005) as the short-dashed curve in Figs. 5 and 6. That curve is based on the analysis of a sample of 355 galaxy images in 21 cm H I emission made as part of the “WHISP” project (Van der Hulst et al. 2001). The distribution of Hubble types in the WHISP sample (Holwerda et al. 2011) is similar to that seen in the complete HIPASS (Zwaan et al. 2003) sample, consisting of about 90% galaxies later than Sb and 10% earlier. However, as noted at the outset of this section, it is limited by a median physical resolution of about 1.4 kpc and the inability to account for opacity effects. The authors suggest that their data might be representative in the range $\log(N_{HI}) = 19.8$ to 21, where sensitivity limits the low end and resolution limits the high end of that range. We plot the extrapolated extension of the fit beyond that range as a dotted line in the figure. Zwaan et al. (2005) have explored the consequences of smoothing of the WHISP data to even coarser resolutions and note that this results in a steepening of the apparent $f(N_{HI}, X)$ for $\log(N_{HI}) = 20 - 21$. Conversely, they expect that achieving higher physical resolution would lead to a flattening of the derived $f(N_{HI}, X)$ in that column density range, which would then more closely resemble what we observe. It

should be noted that the ratio of median beam area between the WHISP sample and ours is a factor of about 400, implying that we sample about three times as many independent beam areas in our sample of only three galaxies as exist in the entire 355 galaxy WHISP sample.

We have attempted to reproduce the effects of coarse physical resolution by smoothing the uncorrected (for opacity) images of our three galaxies to the median beam size of the WHISP sample, 1.4 kpc, and display these in Figure 7. As is clear from a comparison of Figures 1–3 with Figure 7, there is little useful information regarding the statistical occurrence of intrinsic H I column densities at such a coarse physical resolution, given the extensive smearing of intrinsic peaks into larger areas of apparently lower column density. Although the combined distribution function based on these three degraded images yields better agreement with the Zwaan et al. (2005) curve, it still does not agree in detail. Looking at the $f(N_{HI}, X)$ contributions from the individual galaxies, it becomes apparent that the consequence of spatial smearing does not impact all galaxies to the same degree. While the redistribution of actual to apparent column densities has a moderate impact for the larger galactic systems, it becomes more dramatic for physically smaller ones. In the case of the LMC, the apparent area covered by $\log(N_{HI}) = 20 - 21$ gas is increased by about a factor of two by this smoothing. It is likely that this apparent enhancement of such column densities will be even more extreme in lower H I mass systems since they tend to have even smaller physical size. Since low H I mass systems strongly dominate total galaxy numbers, they will similarly influence the distribution function of a galaxy sample via their relative weighting, θ_i in eqn. 4. While we are not able to reproduce the Zwaan et al. (2005) results in detail, it seems likely that the discrepancies are consistent with insufficient physical resolution in the Zwaan et al. study.

Erkal et al. (2012) have presented H I column density distribution functions based on the 34 THINGS galaxy images with physical resolution that varies between about 100 and 500 pc and no ability to include opacity corrections. They compare these to the Zwaan et al. (2005) curve by arbitrarily normalizing the distribution from each THINGS galaxy to the Zwaan et al. curve at $\log(N_{HI}) = 20$, rather than utilizing the space density of each target galaxy. Based on this visual comparison they suggest that the H I distribution function is insensitive to physical resolution as coarse as several kpc. Our own comparison, discussed above and shown in Figs. 5 and 6, utilizes an absolute normalization and clearly demonstrates that both high physical resolution and opacity corrections are vital in recovering the column density distribution function accurately from images of H I 21 cm emission.

The filled circles with error bars in Figure 5 represent the $\langle z \rangle = 0.95$ QSO absorption line data of Rao et al. (2006). The open circles with error bars represent the high redshift QSO absorption line data of Prochaska & Wolfe (2009) and O’Meara et al.

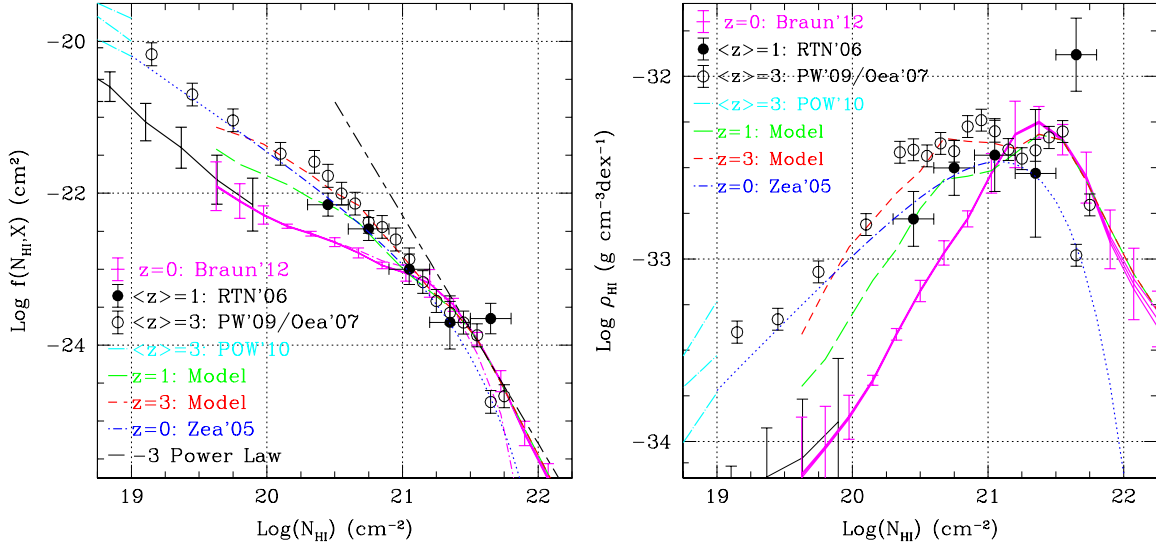


Fig. 6.— Distribution function of neutral hydrogen column density (left) and the mass density function (right) as in Figure 5, but limited to a smaller range in H I column density.

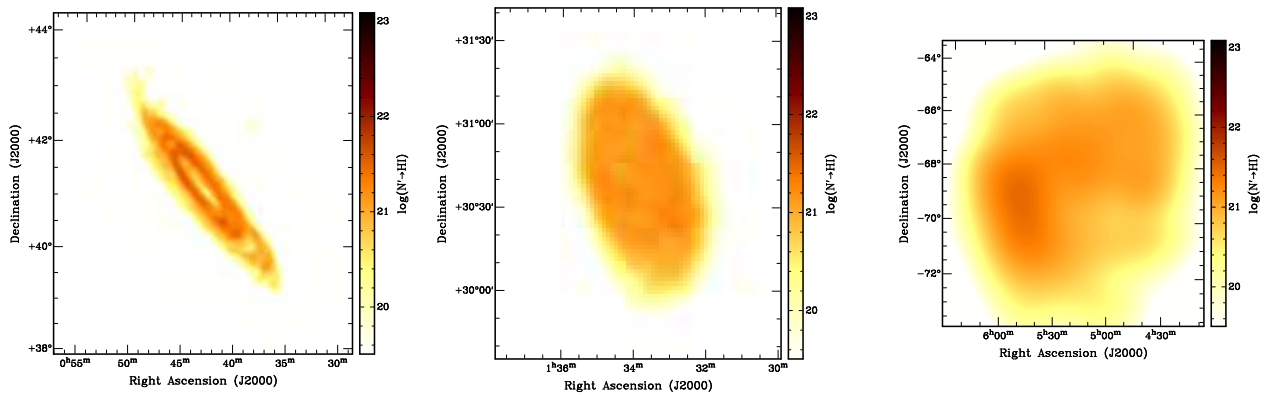


Fig. 7.— Apparent H I column density of M31 (left), M33 (center) and the LMC (right) as seen with an angular resolution that corresponds to 1.4 kpc, the median physical resolution of the “WHISP” survey used in the Zwaan et al. (2005) study.

(2007). Those results are based on a sample of 738 damped Ly α absorption systems (DLA, $\log(N_{HI}) > 20.3$) with $\langle z \rangle = 3.06$ and 78 “Super” Lyman limit systems (SLLS, $19 \leq \log(N_{HI}) \leq 20.3$) with $\langle z \rangle = 3.1$. The $\langle z \rangle = 3.6$ Lyman limit system data (LLS, $17.5 \leq \log(N_{HI}) \leq 19$) from Prochaska et al. (2010) is plotted as the set of dot-long-dash lines. These parameterised fits, taken from Table 5 of Prochaska et al. (2010), represent the range of allowed values. (We note in passing a minor typographical error in one of the tabulated parameters, the constant $\log k_{LLS}$ for one of these curves should likely read -3.1 and not -4.1 .) While the QSO absorption line data is in good agreement with our $z = 0$ distribution function for $\log(N_{HI}) = 21$ to 21.5 , there is an interesting trend apparent for $18 < \log(N_{HI}) < 21$, in which the areal coverage of such intermediate column density neutral gas declines continuously from $z = 3$ to $z = 0$.

Another way of viewing all of the data presented above is to consider the corresponding mass density as function of H I column density. We plot this distribution in the right hand panel of Figure 5. The mass density was calculated from,

$$\rho_{HI}(N_{HI}) = m_H \frac{H_0}{c} f(N_{HI}, X) N_{HI}^2 \ln(10) d\log(N_{HI}) \quad (7)$$

where m_H is the mass of an H I atom. This plot illustrates the range of column density that dominates the contribution to mass density. The trend noted previously for a declining contribution of modest column density gas ($18 < \log(N_{HI}) < 21$) with decreasing redshift is clear. That decline corresponds to about a factor of 5 since $z = 3$ at the DLA limit of $\log(N_{HI}) = 20.3$, and about a factor of 2.5 relative to $z = 1$. The $z = 3.6$ LLS data demonstrate that this excess neutral gas disappears by $\log(N_{HI}) = 17.5$, where the areal coverage converges again with our $z = 0$ distribution function.

The plots of Figure 5 are presented again over a reduced range of column densities in Figure 6 to permit a more detailed comparison of the data and distributions, while the numerical values are listed below in Appendix A for convenience.

Since the primary observed difference between the $z = 0$ and higher redshift H I distribution functions is limited to an increase in the surface area of intermediate column density gas, we have considered a toy model for the $z = 1$ and $z = 3$ images that simply retains the smallest radii in the M31 image shown in Figure 1, and replaces all structures at large projected radii (greater than 25 kpc or 1.8 degree), with the apparent column density version of the same image that is first made fainter by a factor of three ($z = 1$) and five ($z = 3$) and scaled up in linear size by a factor of 1.55 ($z = 1$) and 2.3 ($z = 3$). This could represent an extended intermediate column density halo around the high column density disk, that is larger in area than the actual $z = 0$ galaxy by a factor of 2.4 for $z = 1$ and 5.1 for $z = 3$. The resulting distribution function and mass density function are overlaid on Figs. 5 and 6 as

the long-dashed and short-dashed curves. These curves provide quite a good representation of the QSO absorption line data at $z = 1$ and $z = 3$ of Rao et al. (2006), Prochaska & Wolfe (2009) and O’Meara et al. (2007).

While this toy model is not physically motivated, it serves to demonstrate the types of structures needed to account for the enhanced contributions of intermediate column density gas in the high redshift data, and achieves these with only minimal changes to the $z = 0$ images. Such a distribution might arise if gas accretion rates from the intergalactic medium were substantially enhanced in the past. The recent simulations of Keres et al. (2009) suggest that the total gas accretion rate was enhanced by factors of about 3 and 10 at redshifts of 1 and 3 over that at $z = 0$, with the enhancement of “cold mode” accretion of mildly ionized, 10^{4-5} K gas, being even more dramatic at these redshifts.

An alternative model, that is perhaps more plausible, might consist of a population of dwarf satellites surrounding each massive high redshift galaxy, the majority of which will merge with the parent by $z = 0$. Since the spatial concentration of such a system will be similar to the halo model and the areal coverage of both high and intermediate column density gas will need to be identical (to match the QSO absorption line data) there will likely be only minor practical differences between these two scenarios for the purpose of a statistical description. We have not attempted to pursue modeling of a merging satellite population at this time because of the many additional free parameters that would be introduced.

4.3. H I pathlength functions

A quantity that is often more useful in planning and interpreting surveys is the path-length function, dN/dX , the number of intervening systems per unit co-moving distance along any line-of-sight that exceed a particular column density. This is formed by integrating the positive tail of the H I distribution function and is shown in Figure 8. The two model curves discussed above to represent the $z = 1$ and 3 QSO absorption line data are also plotted in the figure. The total number of equivalent Damped Lyman Alpha (DLA) absorption systems, defined to be those with H I column density, $\log(N_{HI}) > 20.3$, is $n_{DLA}(X, z = 0) = 0.026 \pm 0.003$ for our redshift zero determination. This is almost a factor of two lower than the value estimated by Zwaan et al. (2005), $n_{DLA}(X, z = 0) = 0.045 \pm 0.006$, and seems a consequence of the insufficient physical resolution (a median of 1.4 kpc relative to a structure scale of 100 pc) of that study. Our measurement is compared with the values of $n_{DLA}(X, z)$ published in the studies of Rao et al. (2006) and Prochaska & Wolfe (2009) in the center panel of Figure 8. There has been a continuous decline in $n_{DLA}(X)$ with redshift as noted by many previous authors. Our redshift zero measurement demonstrates an

ongoing decline since $z = 1$, rather than flattening to a constant value as suggested by the Zwaan et al. (2005) point. We include the $n_{DLA}(X, z)$ values of our model for the $z = 1$ ($n_{DLA}(X, z = 1) = 0.042$) and $z = 3$ ($n_{DLA}(X, z = 3) = 0.064$) distributions on the plot to demonstrate the degree to which they are in agreement with the published data. The right-hand panel of Figure 8 presents the redshift evolution of Ω_{HI}^{DLA} , the mass density in H I due to systems with column densities $\log(N_{HI}) > 20.3$. This was calculated for redshift zero by considering the integral mass above this threshold, which amounts to 96% of the total H I mass in galaxies or $\Omega_{HI}^{DLA}(z = 0) = 5.4 \pm 0.9 \times 10^{-4}$. The data points in the figure are those of Rao et al. (2006) (after rescaling to an H I only value) and of Prochaska & Wolfe (2009). For comparison we also plot the mass densities in our redshifted model distributions to demonstrate their consistency.

4.4. Relating 21 cm absorption to H I column density

The 21 cm H I transition offers great promise for documenting the evolution of neutral gas content with cosmic time. However, there are specific issues which need to be overcome before it can fulfill that promise. In the case of 21 cm emission, the issue is sensitivity. Even the deepest integrations with existing facilities have only been able to push back this frontier to $z \sim 0.2$ for individual target detection (Verheijen et al. 2010). And while so-called “stacking” analysis (Lah et al. 2007) can provide some statistical information on gas content at larger distances, the interpretation of such results can not be disentangled from the definition of the sample of objects to be co-added. Reaching down to below M_* on individual targets at redshifts exceeding unity will require about 100 times the sensitivity that is currently available, which can only be achieved with a hundred-fold increase in collecting area such as planned for Phase 2 of the international Square Kilometre Array (Carilli & Rawlings 2004). For 21 cm line absorption, the major limitations are firstly, the need for a large instantaneous field-of-view which would enable effective blind surveys toward background continuum sources and secondly, an effective calibration of integrated absorber strength with the associated H I column density. The limitation of field-of-view is currently being addressed with Phased Array Feed (PAF) technology deployed on parabolic reflectors (DeBoer et al. 2009) that will provide as much as 30 deg² of instantaneous sky coverage. The limitation of 21 cm absorber calibration is one that we will attempt to address here.

The necessity for calibration of the 21 cm absorption line strength is determined by the intrinsic temperature sensitivity of the 21 cm H I line opacity, which varies inversely with temperature, as already noted in eqn. 2 as well as on possible nonthermal contributions to the linewidth. Since any particular line-of-sight is likely to traverse more than one

temperature of medium, there might be no simple correspondence of the 21 cm line opacity with the underlying H I column density. Fortunately, there appears to be a particularly good one-to-one correspondence of these quantities observationally. Kanekar et al. (2011) have recently demonstrated the remarkably tight relationship between integrated 21 cm absorption opacity and the apparent (ie. uncorrected for opacity) column density determined from complimentary 21 cm emission observations of neighbouring lines-of-sight. We present a similar plot in Figure 9 where the Galactic 21 cm absorption and emission data of Kanekar et al. (2011) are plotted as filled circles, together with similar data obtained toward M31 by Braun & Walterbos (1992) as open circles and the LMC by Marx-Zimmer et al. (2000) as open squares. Only the high signal-to-noise absorption detections (exceeding 4σ) are plotted. The curves in the figure represents the expectation for a “sandwich” geometry of cool gas with properties (T_c, τ_c) surrounded by layers of warm gas with properties (T_w, τ_w) as discussed in Kanekar et al. (2011) from,

$$N'_{HI} = N_0 e^{-\tau'_c} + N_\infty (1 - e^{-\tau'_c}) \quad (8)$$

for a measured “apparent” column density, N'_{HI} (based on the integral of observed brightness temperature), a threshold column density (where $\tau_c \rightarrow 0$), $N_0 \sim T_w \tau_w \Delta V$, a saturation column density (where $\tau_c \rightarrow \infty$), $N_\infty \sim (T_c + T_w \tau_w / 2) \Delta V$ and an effective opacity, τ'_c . The effective opacity is related to the measured integrated opacity by the effective linewidth, ΔV , as $\int \tau dV = \tau'_c \Delta V$. The solid curve is for ($N_0 = 1.25 \times 10^{20} \text{ cm}^{-2}$, $N_\infty = 7.5 \times 10^{21} \text{ cm}^{-2}$, $\Delta V = 15 \text{ km/s}$) while the dashed and dot-dash curves are for ($N_0 = 10^{20} \text{ cm}^{-2}$, $N_\infty = 5.0 \times 10^{21} \text{ cm}^{-2}$, $\Delta V = 20 \text{ km/s}$) and ($N_0 = 2 \times 10^{20} \text{ cm}^{-2}$, $N_\infty = 10^{22} \text{ cm}^{-2}$, $\Delta V = 10 \text{ km/s}$), respectively.

The “sandwich” geometry is meant to represent the role of a “temperature-shielding” column density of the Warm Neutral Medium (WNM) that absorbs local EUV and X-ray radiation and is a requirement for condensation of the Cool Neutral Medium (CNM) within (e.g. Wolfire et al. 2003). It should be noted that this “temperature-shielding” column is quite distinct from the “self-shielding” column density of only a few times 10^{17} cm^{-2} that marks the onset of recombination of hydrogen within an ionizing radiation field (e.g. Dove & Shull 1993). Once neutral columns of about 10^{19} cm^{-2} are achieved, the expectation is that the ionization fraction will be minimal, even in extreme radiation fields. Such a model provides a very good characterisation of the observable properties of the absorbing medium in the Galaxy, where it is best constrained by data, but also of the available extragalactic data from M31 and the LMC, in which both higher and lower metallicity and radiation field environments are probed. The dashed and dot-dash curves provide a reasonable estimate of the scatter observed in this relationship. Since the curves drawn in Figure 9 are based on a physical model, we can also write the corresponding equation for the *actual rather than the*

apparent H I column density,

$$N_{HI} = N_0 + (N_\infty - \frac{N_0}{2})\tau'_c \quad (9)$$

The curves based on the same parameters as previously are drawn in the right-hand panel of Figure 9. While these are unchanged at low column density, they do not exhibit the saturation effect at high columns that afflict observations of 21 cm H I emission.

4.5. 21 cm opacity distribution function

With the column density calibration of 21 cm absorption line strength of the previous sub-section in hand it becomes possible to construct the distribution function of 21 cm opacity. Eqn. 9 was used to transform the three images of opacity-corrected column density (Figs. 1–3) to corresponding images of 21 cm absorption line strength. The transformation was done using the nominal transformation depicted in Figure 9 with parameters ($N_0 = 1.25 \times 10^{20} \text{ cm}^{-2}$, $N_\infty = 7.5 \times 10^{21} \text{ cm}^{-2}$, $\Delta V = 15 \text{ km/s}$) as well as the two envelope curves with ($N_0 = 10^{20} \text{ cm}^{-2}$, $N_\infty = 5.0 \times 10^{21} \text{ cm}^{-2}$, $\Delta V = 20 \text{ km/s}$) and ($N_0 = 2 \times 10^{20} \text{ cm}^{-2}$, $N_\infty = 10^{22} \text{ cm}^{-2}$, $\Delta V = 10 \text{ km/s}$) in order to track the intrinsic scatter and uncertainty. The distribution function was then calculated from eqn. 4 but with $\int \tau dV$ in the place of N_{HI} . This is shown in Figure 10 with the solid curve illustrating the nominal $z = 0$ relation, while the dashed and dot-dashed curves span the scatter and uncertainty. What is notable is the flatness of the distribution below about $\int \tau dV = 0.1 \text{ km s}^{-1}$. The “temperature-shielding” threshold implies that there will be essentially no additional systems seen with an intrinsic absorption depth below this value.

Distribution functions of the 21 cm absorption for the toy models developed above to describe the $z = 1$ and 3 QSO data are also plotted in Figure 10 as the dotted and short-dashed curves utilizing the nominal $z = 0$ transformation. There is considerable uncertainty in the applicability of the $z = 0$ relation at these higher redshifts. The intergalactic ionizing radiation field is expected to increase dramatically with redshift in concert with the evolution of the massive star formation rate and active galaxy incidence. While this will have a major influence on the “self-shielding” column density (of a few times 10^{17} cm^{-2}) for the onset of the ionized to neutral transition at the galaxy-IGM interface, it is less clear what the impact might be on the “temperature-shielding” column (of $\sim 10^{20} \text{ cm}^{-2}$) for the warm to cool transition that occurs deep within individual galaxy disks. This is because the radiation field in this latter case is strongly dominated by local contributions (e.g. Wolfire et al. 2003). It is likely that the intrinsic scatter of the $z = 0$ relation in Figure 9 is already a consequence of the large variations in local radiation field intensity that naturally occur within individual

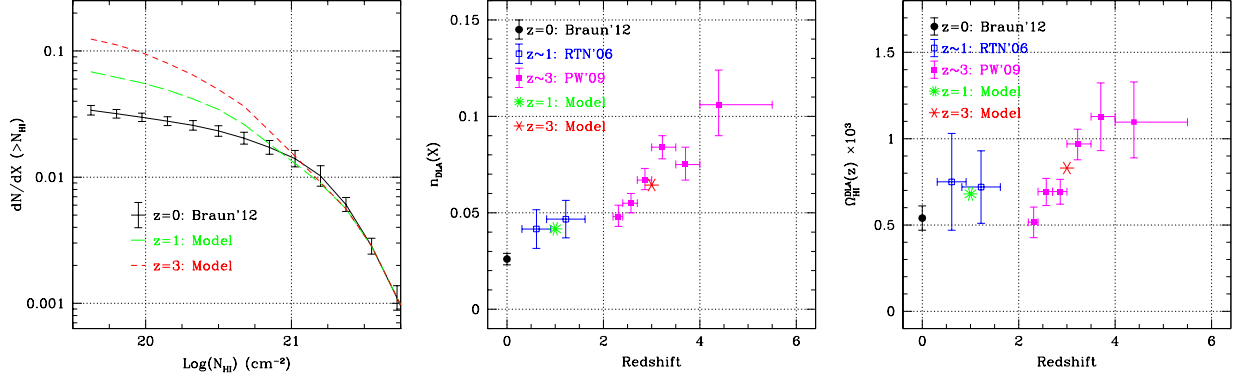


Fig. 8.— Pathlength function of H I column density (left), as well as redshift evolution of the total number (center) and H I mass density (right) of DLA systems.

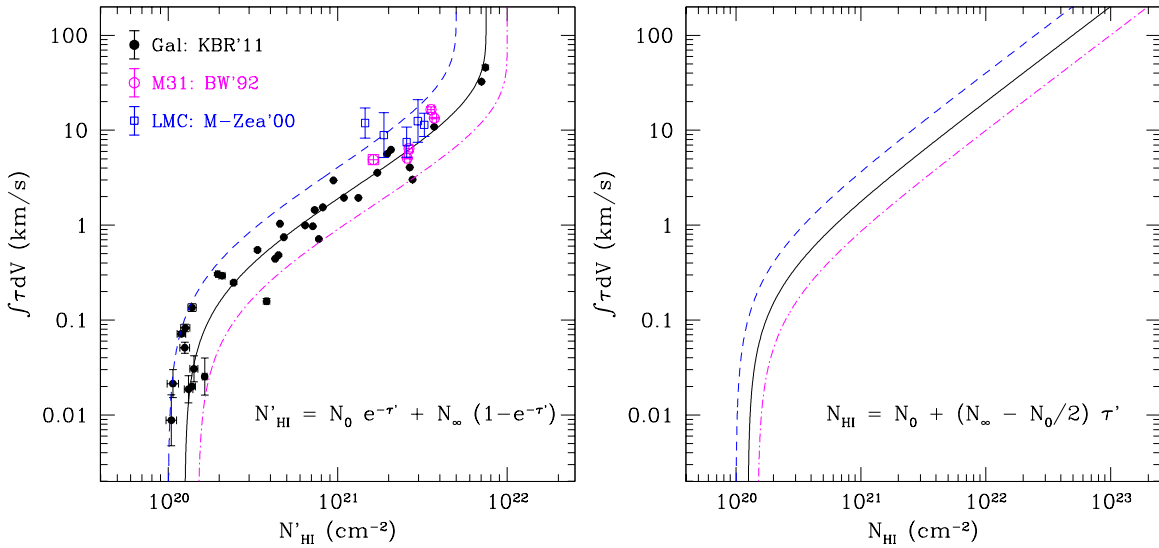


Fig. 9.— The relation of integrated 21 cm absorption with apparent neutral hydrogen column density (left) and total neutral hydrogen column density (right).

galaxies. Future work will be vital to test this hypothesis in more extreme environments, such as the disks of nearby star-bursting galaxies. We will continue with our discussion of possible evolutionary trends of absorption properties with this caveat in mind.

Since deep 21 cm absorption features, $\int \tau dV > 5 \text{ km s}^{-1}$, require high column density, $N_{\text{HI}} > 10^{21.3} \text{ cm}^{-2}$, lines-of-sight and the incidence of such column densities does not appear to evolve significantly with redshift (Figure 6), there is also no evolution in the distribution function of 21 cm absorption in Figure 10 for such deep features. Redshift evolution is confined to the relatively weak 21 cm absorbers with strength $\int \tau dV < 1 \text{ km s}^{-1}$ that correspond to $N_{\text{HI}} < 10^{21} \text{ cm}^{-2}$.

4.6. The pathlength function of 21 cm absorption

Just as was done above for the H I column density, it is possible to calculate the corresponding pathlength function, dN/dX , the number of 21 cm absorption systems per unit distance that exceed a particular absorption depth, $\int \tau dV$. This is formed by integrating the positive tail of the 21 cm absorption distribution function and is shown in Figure 11 with the same curves used previously to depict the $z = 0, 1$ and 3 predictions. The same trends noted previously for the distribution function apply here as well, namely an absence of redshift evolution for deep absorbers and number evolution by a factor of several for the faint absorbers.

4.7. The impact of finite background source size

The preceding discussion has assumed that the background source used to probe intervening absorbers has a small angular size relative to the most compact structures within the absorbing system. What if this is not the case? Since we already have images that represent absorption depth, it is straightforward to simulate the observable effect of an arbitrary background source size and structure. This can be done by evaluating the convolution of the absorption depth image with an image of the background source, normalized to preserve the integrated absorption depth. The distribution function of such convolved images can then be calculated in the same way. This has been done in the right hand panels of Figs. 10 and 11 for an assumed Gaussian background source of 9 kpc FWHM. This choice of background source model is motivated by the 1.3 arcsec median source size observed for mJy brightness radio sources at GHz frequencies (Windhorst 2003) which subtend more than 9 kpc for all redshifts greater than about 0.7. This should be regarded as a “worst case scenario” from

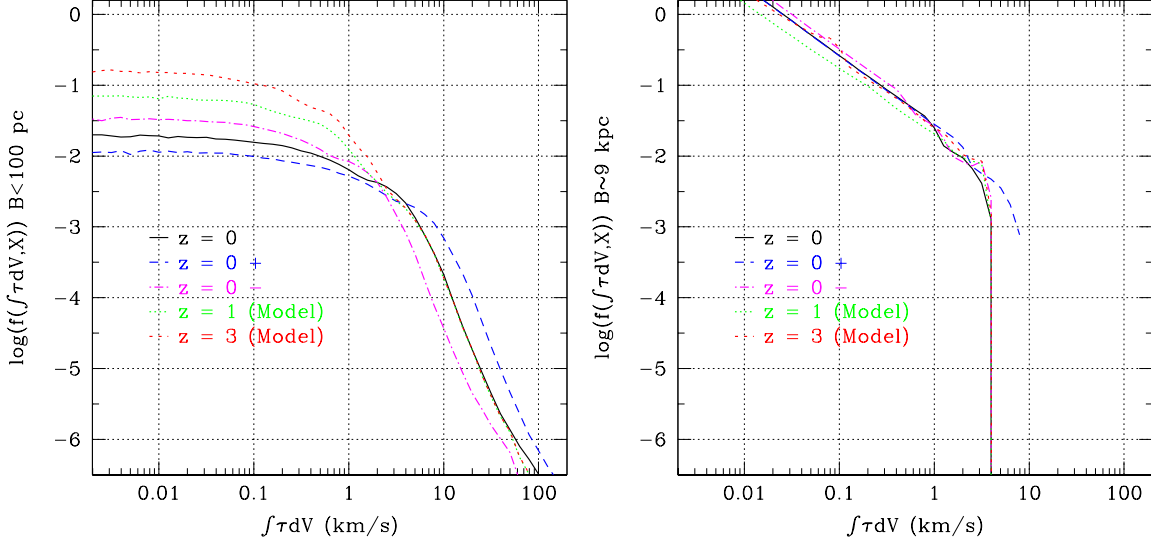


Fig. 10.— Distribution function of integrated 21 cm absorption at full resolution (left) and observed with 9 kpc effective resolution (right).

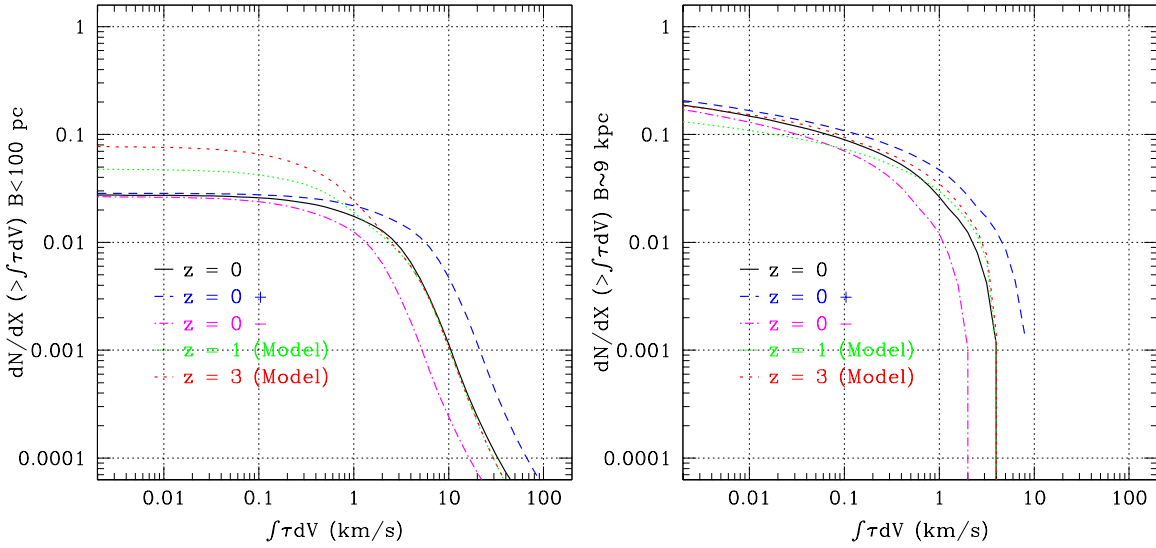


Fig. 11.— Pathlength function of integrated 21 cm absorption observed at full resolution (left) and observed with 9 kpc effective resolution (right).

the standpoint of absorption signal dilution, since there is some probability that a compact component may be present, even in an intrinsically extended background source.

The impact of a significantly extended background source on the 21 cm absorber distribution and pathlength functions is dramatic. As can be seen in the right hand panels of Figs. 10 and 11, deep absorption systems will not be observed at all in this instance, while an enhanced number of apparently faint absorbers are seen instead. This redistribution of intrinsically deep into apparently faint absorbers also has as a consequence that there is no predicted observable evolution at all in the 21 cm absorption properties with redshift.

As noted above, this assessment must be regarded as a “worst case scenario” since the median source size has been distributed smoothly in our simulation. Better insights into the typical structures seen in radio sources at GHz frequencies are provided by the recent study of Middelberg et al. (2011) who studied a sample of nearly 100 moderate brightness radio sources with angular resolution of about 20 mas. Overall, some 20% of these sources were found to have a substantial (50 – 100%) flux contribution from unresolved structures. However, when considering sources fainter than 1 mJy at 1.4 GHz, this fraction declined to only 7%.

What the dramatic contrast between the left- and right-hand panels of Figs. 10 and 11 underlines is the importance of isolating the flux contribution of suitably compact structures, subtending less than about 100 pc at the distance of the absorption system, in interpreting any measurement of 21 cm absorption. Interpretation is essentially impossible without this information. The implication for large surveys of H I 21 cm absorption at redshifts $z > 0.5$ is that high resolution imaging, with about 15 mas beam size, will be needed for the useful interpretation of any detections, either during the survey itself or as follow-up. At the relevant observing frequencies, $\nu < 700$ MHz, this implies a need for baselines greater than about 5500 km.

5. Conclusions

The analysis of high resolution and sensitivity H I datacubes of Local Group galaxies has permitted some fundamental conclusions to be drawn:

1. Galaxy disks contain a significant population of H I features which are self-opaque in the 21 cm transition. Such features are intrinsically compact, with narrow dimensions that are typically only about 100 pc, which determines the resolution required for their study. Such features can locally disguise the presence of high atomic column densities in the range $22 < \log(N_{HI}) < 23$, that are not apparent in images of the integrated

21 cm linestrength. Globally, such features account for about $34\pm 5\%$ more atomic gas than is derived under the assumption of negligible self-opacity.

2. Application of this opacity correction to recent estimates of the cosmological mass density of H I within local galaxies yields, $\Omega_{HI}^{gal}(z = 0) = 5.6\pm 0.9 \times 10^{-4}$ assuming that our limited galaxy sample provides a representative determination.
3. The resolved, opacity corrected images of Local Group galaxies permit calculation of a robust redshift zero H I distribution function, $f(N_{HI}, X)$, with excellent statistical properties (based on 1000's of independent sight-lines) and a high degree of internal consistency amongst galaxy types between Sb and Sm. While similar to high redshift determinations, there is evidence for a systematic decline in intermediate column density gas, $18 < \log(N_{HI}) < 21$, that can be well modelled by a decrease in the surface area of galaxy halos (or associated satellites) by a factor of about 2.5 since $z = 1$ and a factor of about 5 since $z = 3$.
4. The number of equivalent Damped Lyman Alpha (DLA) H I absorbers per unit comoving length, $n_{DLA}(X, z = 0) = 0.026\pm 0.003$, is significantly lower than seen at higher redshifts by factors as large as about four and follows a smoothly declining trend. Similarly, the cosmological mass density in DLAs, $\Omega_{HI}^{DLA}(z = 0) = 5.4\pm 0.9 \times 10^{-4}$, follows a smoothly declining trend, albeit one that sees only a factor of two decline between redshift 4 and the present.
5. There is a tight, non-linear correlation between the observed 21 cm absorption opacity and the integrated 21 cm emission brightness from adjacent sight-lines through nearby galaxy disks which permits “calibration” of our H I column density images into corresponding ones of integrated 21 cm opacity.
6. We present predictions for the distribution and pathlength functions of 21 cm integrated opacity at both redshift zero and at high redshift for the case of no evolution in the local opacity calibration. The prediction is that faint 21 cm absorbers, $\int \tau dV < 1 \text{ km s}^{-1}$, have declined by a factor of about 2.5 since $z = 1$ and a factor of about 5 since $z = 3$, while the number of deep absorbers, $\int \tau dV > 5 \text{ km s}^{-1}$, has not evolved.
7. We explore the impact of a finite background source size on the distribution and pathlength functions of 21 cm integrated opacity. Adoption of the observed 1.3 arcsec median source size of mJy radio sources dramatically changes the apparent opacity distributions and effectively precludes any physical interpretation of the measurements. Future surveys of 21 cm absorption will require a 15 mas beamsize for their unambiguous interpretation.

We acknowledge the useful comments of Jason Xavier Prochaska, Elaine Sadler and Dave Thilker on an earlier version of this manuscript. The Westerbork Synthesis Radio Telescope is operated by ASTRON (Netherlands Foundation for Research in Astronomy) with support from the Netherlands Foundation for Scientific Research (NWO). The National Radio Astronomy Observatory, which operates the Green Bank Telescope and Very Large Array, is a facility of the National Science Foundation operated under cooperative agreement by Associated Universities, Inc. The Australia Telescope and the Parkes are funded by the Commonwealth of Australia for operation as a National Facility managed by CSIRO.

Facilities: WSRT, VLA, ATCA, Parkes, GBT.

A. Numerical values of the redshift zero H I distribution function

The numerical values of the H I distribution function presented in this paper are tabulated below. The data source for the different column density ranges are indicated. The error estimates in the third column are determined from the number of independent image pixels used in the evaluation for the data of references 1 and 2, while for reference 3 this is determined from the RMS deviation amongst the three contributing galaxies, which exceeds the statistical error estimate by factors of between four and 20.

Table 2. H I distribution function at $z = 0$

$\log(N_{HI})[\text{cm}^{-2}]$	$\log(f(N_{HI}, X))$	$\Delta\log(f(N_{HI}, X))$	Ref
16.75	-17.28	0.093	1
17.00	-17.43	0.083	1
17.25	-17.74	0.089	1
17.50	-18.38	0.140	1
17.75	-18.82	0.174	1
18.00	-19.25	0.213	1
18.25	-19.69	0.265	1
18.50	-20.14	0.334	1
18.75	-20.44	0.353	1
18.58	-20.30	0.188	2
18.84	-20.60	0.195	2
19.11	-21.06	0.246	2
19.37	-21.40	0.269	2
19.63	-21.82	0.322	2
19.89	-22.15	0.348	2
19.62	-21.91	0.321	3
19.80	-22.10	0.227	3
19.97	-22.29	0.121	3
20.15	-22.43	0.027	3
20.32	-22.53	0.032	3
20.50	-22.64	0.058	3
20.67	-22.79	0.067	3
20.85	-22.95	0.044	3
21.02	-23.05	0.109	3
21.20	-23.19	0.182	3
21.37	-23.47	0.086	3
21.55	-23.92	0.084	3
21.73	-24.47	0.139	3
21.90	-25.16	0.161	3
22.07	-25.76	0.195	3
22.25	-26.30	0.152	3

REFERENCES

- Bernard, J.-P., Reach, W.T., Paradis, D., et al. 2008, *AJ*, 136, 919
- Braun, R., Walterbos, R.A.M, 1992, *ApJ*, 386, 120
- Braun, R., 1995, *A&AS*, 114, 409
- Braun, R., 1997, *ApJ*, 484, 637
- Braun, R., Thilker, D.A., 2004, *A&A*, 417, 421
- Braun, R., Kanekar, N., 2005, *A&A*, 436, L53
- Braun, R., Thilker, D.A., Walterbos, R.A.M, Corbelli, E., 2009, *ApJ*, 695, 937
- Carilli, C.L., Rawlings, S., 2004, *New Astr.Rev.* 48, 979
- DeBoer, D.R., Gough, R.G., Bunton, J.D. et al., 2009, *IEEEEP*, 97, 1507
- Dickman, R.L., Snell, R.L., Schloerb, F.P., 1986, *ApJ*, 309, 326
- Dove, J.B., Shull, J.M., 1994, *ApJ*, 423, 196
- Erkal, D., Gnedin, N.Y., Kravtsov, A.V., 2012, 2012arXiv1201.3653E
- Ewen, H.I., Purcell, E.M., 1951, *Nature*, 168, 356
- Fynbo, J.P.U., Jakobsson, P., Prochaska, J.X., et al. *ApJSS*, 185, 526
- Gordon, K.D., Bailin, J., Engelbracht, C.W., et al. 2006, *ApJ*, 638, L87
- Gratier, P., Braine, J., Rodrogez-Fernandez, N.J. et al., 2010, *A&A*, 522, 3
- Hagen, J.P., McClain, E.F., 1954, *ApJ*, 120, 368
- Heald, G., Josza, G., Serra, P., et al., 2011 *A&A*, 526, A118
- Henderson, A.P., Jackson, P.D., Kerr, F.J., 1982, *ApJ*, 263, 116
- Hinshaw, G., Weiland, J.L., Hill, R.S., et al., 2009, *ApJS*, 180, 225
- Holwerda, B.W., Pirzkal, N., de Blok, W.J.G. et al., 2011, *MNRAS*, 416, 2437
- Kanekar, N., Braun, R., Roy, N., 2011, *ApJ*, 737, L33
- Keres, D., Katz, N., Fardal, M., Dave, R., Weinberg, D.H., 2009, *MNRAS*, 395, 160

- Kim, S., Staveley-Smith, L., Dopita, M.A., et al. 2003, ApJS, 148, 473
- Koerwer, J.F., 2009, AJ 138, 1
- Lah, P., Chengalur, J.N., Briggs, F.H., et al. 2007, MNRAS, 376, 1357
- Martin, A.M., Papastergis, E., Giovanelli, R. et al., 2010, ApJ, 723, 1359
- Marx-Zimmer, M., Herbstmeier, U., Dickey, J.M., et al., 2000, A&A, 354, 787
- McConnachie, A.W., Irwin, M.J., Ferguson, A.M.N., et al. 2004, MNRAS, 350, 243.
- McConnachie, A.W., Irwin, M.J., Ferguson, A.M.N., et al. 2005, MNRAS, 356, 979.
- Middelberg, E., Deller, A., Morgan, J., et al. 2011, A&A, 526, A74.
- Milgrom, M., 1988, A&A, 202, L9
- Muller, C.A., Oort, J.H., 1951, Nature, 168, 357
- O’Meara, J.M., Prochaska, J.X., Burles, S., et al., 2007, ApJ, 656, 666
- Prochaska, J.X., Wolfe, A.M., 2009, ApJ, 696, 1543
- Prochaska, J.X., O’Meara, J.M., Worseck, G., 2010, ApJ, 718, 392
- Radhakrishnan, V., 1960, PASP, 72, 427
- Rao, S., Briggs, F., 1993, ApJ, 419, 515
- Rao, S.M., Turnshek, D.A., Nestor, D.B., 2006, ApJ, 636, 610
- Rohlf, K., Braunsfurth, E., Mebold, U. 1972, AJ, 77, 711
- Ryan-Weber, E.V., Wabster, R.L., Staveley-Smith, L., 2003, MNRAS, 343, 1195
- Schmidt, M., 1957, Bull.Astron.Inst.Netherlands, 13, 247
- Schmidt, M., 1959, ApJ, 129, 243
- Thilker, D.A., Braun, R., Walterbos, R.A.M., 2002, ASP Conf. Ser. Vol. 276, p.370
- Thilker, D.A., Braun, R., Walterbos, R.A.M. et al., 2004, ApJL, 601, 39
- Thilker, D.A., Braun, R., Fukui, Y., et al., 2012, ApJ, in preparation
- van der Hulst, J.M., van Albada, T.S., Sancisi, R., 2001, ASP Conf. Ser. Vol. 240, p.451

Verheijen, M., Deshev, B., van Gorkom, J. et al., 2010, Proc.Sci.

Walter, F., Brinks, E., de Blok, W.J.G., et al., 2008, AJ, 136, 2563

Windhorst, R.A., 2003, New Astr.Rev. 47, 357

Wolfire, M.G., McKee, C.F., Hollenbach, D., Tielens, A.G.G.M., 2003, ApJ, 587, 278

Zwaan, M.A., Staveley-Smith, L., Koribalski, B.S., et al., 2003, AJ, 125, 2842

Zwaan, M.A., Van der Hulst, J.M., Briggs, F.H., et al., 2005, MNRAS, 364, 1467

Table 2—Continued

$\log(N_{HI})[\text{cm}^{-2}]$	$\log(f(N_{HI}, X))$	$\Delta\log(f(N_{HI}, X))$	Ref
22.43	-26.73	0.161	3
22.60	-27.09	0.315	3
22.77	-27.52	0.332	3
22.95	-28.25	0.461	3

References. — (1) Braun & Thilker 2004; (2) Thilker et al. 2004; (3) Current study